

# Numerical Simulation of Blast-Induced Fracturing of Jointed Rock Masses Based on a Case Study<sup>1</sup>

Magreth S. Dotto and Yashar Pourrahimian  
Mining Optimization Laboratory (MOL)  
University of Alberta, Edmonton, Canada

## ABSTRACT

*Fragmentation by blasting is a critical process in hard rock mining. The interaction between the rock mass and blast energy influences the outcomes, specifically on the rock mass response to higher stresses and loading rates and the influence of structures. Each rock mass is unique, but some features affect the blast energy similarly, leading to similar outcomes. Having analyzed these features and their influence on blast outcomes, they can be addressed during the blast design to achieve better results. In this study, the Riedel-Hiermaier-Thoma (RHT) material model in L-S DYNA is used to model the nonlinear dynamic fracturing of the rock to understand the effects of rock mass properties on the blast outcomes. In a case study, rock mass properties, explosive properties, and design parameters are used as input parameters to the model, and the blast outcomes are used to validate simulation results. The results show that several factors influence the fracturing process by blasting. The formation of damage zones around the charge among others depends on the rock mass strength and structural properties which control energy distribution and crack propagation. Furthermore, the simulation results indicate that when the model parameters are calibrated from the existing data, they can be used to simulate the fragmentation process in a more simplified and controlled environment and therefore provide insight into blast design.*

## 1. Introduction

Blasting is a commonly used method of rock fragmentation in mining and civil engineering constructions. Although it is the most efficient way of breaking the rock, it is a complicated process mainly due to the complex nature of the rock mass, the non-ideal detonation of commercial explosives, the interaction between the rock mass and explosive energy, and the interaction with the neighboring charges. The efficiency of the blasting process is measured by how loose and well-fragmented the rock is while managing the overall production costs and limiting the impacts on the surrounding structures. To achieve blast efficiency, understanding the physical and mechanical properties of the rock mass and blasting mechanisms is essential.

Several approaches have been developed to describe blast-induced fragmentation and thus estimate damage zones ranging from analytical [1], experimental [2] to numerical modeling [3-6]. The analytical approach uses parameters such as peak particle velocity (PPV) [7, 8] or borehole pressure [9] to estimate the damage zones. Numerical modeling uses algorithms such as the Discrete Element Method (DEM), Finite Element Method (FEM), etc., to analyze stress fields around the charge and estimate the damage zones. These approaches have come up with valuable insights into the

---

<sup>1</sup> A version of this paper is submitted to the International Journal of Mining, Reclamation, and Environment.

interaction between explosive energy and rock mass; they still are not exhaustive, especially when considering heterogeneous, anisotropic, and discontinuous rock mass.

In the rock mass, discontinuities such as fractures, joints, and faults are common. The knowledge of their geometric and structural attributes is vital in earth science studies, particularly stress wave propagation [10-12]. These discontinuities are known to alter rock mass fracture patterns in quasi-static loading and affect the propagation of stress waves, and the formation and propagation of cracks in dynamic loading. Several studies have been conducted to study wave propagation in the rock mass and the effects of rock joints through site monitoring and numerical simulations [13-20]. These studies concluded that the intensity of the stress wave at any point around the charge depends on the size of the charge, rock mass properties, and the distance from the blast hole. The stress wave attenuates faster near the charge and slower with increased distance from the blast hole. The presence of joints in the rock mass influences the attenuation and distribution of explosive energy depending on the properties of the joints and their orientation to the direction of the wave front.

This study presents the results of the numerical simulation of blasts using the LS-DYNA [21] for the intact and jointed rock mass, considering various joint parameters and structural properties. The simulation model is first calibrated from the rock mechanical properties, joint parameters, and explosive properties of an existing mine. Empty joints (with air as filling material) and joints filled with soft rock material (clay) are modeled to evaluate the effect of filling material on the distribution of wave energy and rock fracturing. Further analysis is conducted on different joint parameters, such as thickness, orientation, spacing, and joint set orientation when soft rock is the filling material. This analysis aims to investigate their influence on stress wave propagation and the creation of damage zones around the blast hole. The results are compared with post-blast field measurements from a similar setup through fragmentation analysis. The study is essential in understanding the interaction of explosive energy with the rock mass to predict the blast outcomes and aid blast design.

## 2. Numerical Modeling

Numerical modeling, both finite element modeling (FEM) [22, 23] and discrete element modeling (DEM) [5, 6] have been used as the most economical and effective techniques to simulate the blasting process and optimize blast fragmentation. In DEM, the rock mass is represented as an assembly of bonded elements with specified tensile or shear strength. Failure is achieved when the stress exceeds this value [5]. This approach can successfully track crack evolution and fracture patterns, but without some modifications and assumptions, it falls short in tracking explosive gas dispersion, as noted by Yoon and Jeon [5]. In FEM, the damage mechanics is due to the growth and nucleation of cracks in the brittle rock mass defined by the appropriate damage evolution law [24].

Most blast-induced fragmentation studies are based on two dimensions (2D) analysis. Although they simplify the computation process and provide a significant understanding of the fragmentation process and the influence of discontinuities, they do not capture the spatial stress distribution and blast damage in the three-dimensional (3D) setup. This study investigates 2D and 3D numerical simulation models for a single blast hole in various applications. In both cases, the reference model is an intact rock whose outcomes are compared with jointed rock mass to analyze the effects of various joint parameters.

LS-DYNA, a nonlinear transient finite element code with an explicit integration scheme capable of implementing dynamic problems, is used for blasting modeling. LS-DYNA can successfully model the interaction between the solid material and fluid and gas flow using the Lagrangian algorithm and Arbitrary Lagrangian-Eulerian (ALE). LS-DYNA can incorporate coupling between the Lagrangian and ALE interface when required. Boundary conditions to restrict elements' movements can also be applied as needed. Two main damage models commonly used to simulate the damage evolution of rock mass under blasting loads in LS-DYNA are the Holmquist–Johnson–Cook (HJC) model [25] and the Riedel–Hiermaier–Thoma (RHT) model [26]. From the study conducted by Wang [27], the

RHT model is observed to define damage distribution in rock well and describe the formation of the crushed zone and propagation of radial tensile cracks, while the latter could not be captured in the HJC model

### 2.1. The RHT material model

The rock is modeled with the Riedel-Hiermaier-Thoma (RHT) material model, an advanced brittle plasticity model for impulsive and dynamic loadings. The RHT model has been used extensively to model blast-induced fragmentation [27-29] since the rock has numerous randomly distributed pores and micro-cracks and behaves nonlinearly under compression. The RHT material strength model is coupled with a polynomial Equation of State (EOS) that accounts for porous compaction as expressed in Equation (1); where  $B_0$  and  $B_1$  are constants for polynomial EOS,  $\alpha_0$  is the initial porosity,  $\rho_0$  is the rock density,  $e$  is the internal energy per unit mass,  $\mu$  is the volumetric strain and  $A_1$ ,  $A_2$ , and  $A_3$  are Hugoniot polynomial coefficients.

$$P_{EOS} = \frac{1}{\alpha} \left( (B_0 + B_1 \mu) \alpha_0 \rho_0 e + A_1 \mu + A_2 \mu^2 + A_3 \mu^3 \right) \quad (1)$$

Figure 1 describes the p- $\alpha$  compaction model. Pore crush pressure ( $P_{crush}$ ) and compaction pressure ( $P_{comp}$ ) define failure modes in the model. Below the  $P_{crush}$ , the model is elastic. Beyond  $P_{crush}$ , with pressure increase, porous compaction occurs accompanied by a reduction in the effective bulk modulus of the material and volumetric stiffness. When the pressure reaches the  $P_{comp}$ , the material is fully compacted, and the conventional equation of the state model governs the damage evolution [30].

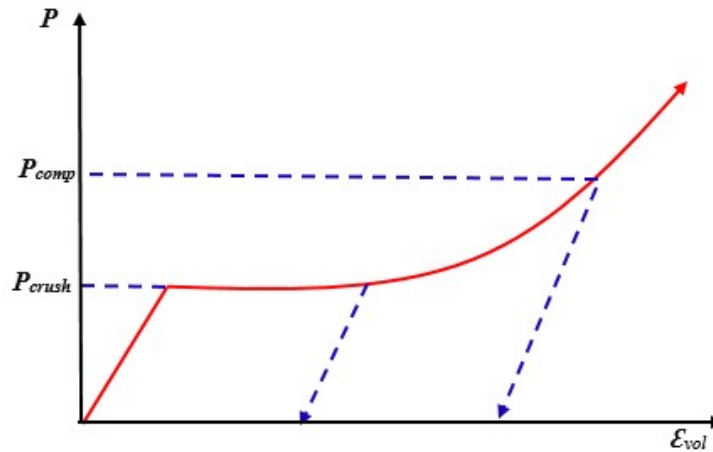


Figure 1. P-Q equation of state [30].

Three limit surfaces define the RHT strength model; the initial elastic yield surface, residual friction surface, and failure surface, which depend on the hydrostatic pressure. The damaged surfaces represent the reduction in material strength in different meridians and the effect of strain rate. Surface material failure is achieved when its ultimate compressive, shear, or tensile strength is reached. Figure 2 illustrates an example of static compressive meridian surfaces. Figure 2 shows that the model is elastic until it reaches the initial yield surface, beyond which plastic strain prevails. The elastic-plastic yield surface in compression is defined by compressive strength, regularized yield function, which describes pressure dependence on principal stress conditions, and William-Warke function, representing reduced strength on shear and tensile meridian presented in Equation (2).

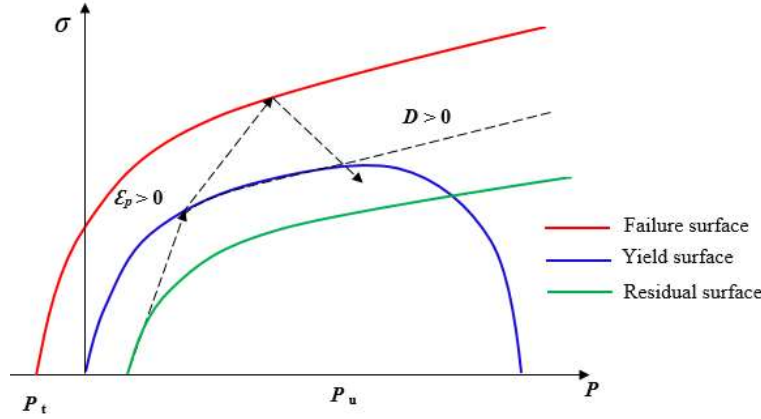


Figure 2. Stress limit surfaces and loading scenario [30].

$$\sigma_y \left( P_o^*, \varepsilon_p^*, \varepsilon_p^* \right) = f_c \sigma_y^* \left( P_o, F_r \left( \varepsilon_p^* \right), \varepsilon_p^* \right) R_3 \left( \theta_l, P_o^* \right) \quad (2)$$

Where  $\sigma_y^*$  is the normalized yield function ( $\sigma_y^* = \sigma_y / f_c$ ),  $f_c$  is uniaxial compressive strength,  $P_o^*$  is the normalized pressure ( $P_o^* = P_o / f_c$ ),  $P_o$  is hydrostatic pressure,  $F_r$  is the dynamic strain rate increase factor,  $\varepsilon_p^*$  is the strain rate,  $\varepsilon_p^*$  is the effective plastic strain,  $R_3$  is William Warnke function, and  $\theta_l$  is lode angle. The strain rate affects the strength of the rock. Equation (3) defines the rate dependency.

$$F_r(\varepsilon_p) \begin{cases} \left( \frac{\varepsilon_p^*}{\varepsilon_o^{*c}} \right)^{\beta_c} & P \geq f_c / 3 \\ \frac{P + f_t / 3}{f_c / 3 + f_t / 3} \left( \frac{\varepsilon_p^*}{\varepsilon_o^{*t}} \right)^{\beta_c} - \frac{P - f_c / 3}{f_c / 3 + f_t / 3} \left( \frac{\varepsilon_p^*}{\varepsilon_o^{*c}} \right)^{\beta_t} & -f_t / 3 < P < f_c / 3 \\ \left( \frac{\varepsilon_p^*}{\varepsilon_o^{*t}} \right)^{\beta_t} & P \leq -f_t / 3 \end{cases} \quad (3)$$

Where  $\varepsilon_o^{*c}$  is the reference strain rate in compression =  $3 \times 10^{-5} \text{ s}^{-1}$  and  $\varepsilon_o^{*t}$  is the reference strain rate in tension =  $3 \times 10^{-6} \text{ s}^{-1}$ ,  $f_t$  is tensile strength and  $\beta_c$  and  $\beta_t$  are material constants in compression and tension, respectively [30]. The failure surface is given by Equation (4).

$$\sigma_f^* \left( P_o^*, F_r \right) = A_l \left( P_o^* - F_r / 3 + \left( A_l / F_r \right)^{-1 / N_l} \right)^{N_l} \quad 3P_o^* \geq F_r \quad (4)$$

Where  $\sigma_f^*$  is normalized strength and  $N_l$  and  $A_l$  are failure surface parameters. Under blast loads, reduction in material strength is governed by relative pressure;

$$Q \left( P_o^* \right) = Q_o + B P_o^* \quad (5)$$

Where  $Q_o$  is the ratio between tensile and compressive radii meridians and  $B$  is the lode angle dependency factor. When stress reaches the failure surface, damage strain accumulation governs damage evolution. The damage variable of the RHT model ( $D$ ) is calculated using Equation (6).

$$D = \sum \frac{\Delta \varepsilon_m^P}{\varepsilon_f^P} \quad (6)$$

Where  $\varepsilon_m^p$  is the accumulated plastic strain and  $\varepsilon_f^p$  the plastic strain failure.  $D$  takes a value between 0 and 1 where  $D = 0$  is the un-damaged material state and  $D = 1$  is the damaged material. Wang, Wang (27) defined the damage pattern from blasting as the elements with a damage level above 0.7. The plastic strain at failure is calculated using Equation (7).

$$\varepsilon_f^p \begin{cases} D_1 (P_o^* - (1 - D)P_t^*)^{D_2} & P_o^* \geq (1 - D)P_t^* + (\varepsilon_m^p / D_1)^{\frac{1}{D_2}} \\ \varepsilon_m^p & P_o^* < (1 - D)P_t^* + (\varepsilon_m^p / D_1)^{\frac{1}{D_2}} \end{cases} \quad (7)$$

Where  $P_t^*$  is failure cut-off pressure,  $D_r$  is the RHT model's damage variable, and  $D_1$ ,  $D_2$  are damage constants. More references on the RHT model can be found in Livermore Software Technology Corporation [21] and Borrvall and Riedel [30].

### 3. Rock Properties and Blast Design Parameters for the Case Study

This study uses the blast design, rock mass, and explosive properties of Geita Gold Mine (GGM), Nyankanga Pit in Tanzania, for modeling. Nyankanga Geology comprises a banded iron formation (BIF) and diorite as host rocks. Mineralization is controlled by tectonic structures within fault zones passing through the host rock. The banded iron formation is of sedimentary origin, consisting of cyclic deposition of iron-rich sediments and chert. The diorite is igneous with variable mineral composition and grain size, defining the Nyankanga Intrusive Complex. The principal composition of the Nyankanga diorite is plagioclase-rich diorite (DPH) and hornblende-rich diorite (DHP). Porphyry intrusions within the fault zones are the youngest Nyankanga geology. The intrusions are mainly feldspar porphyry (FP) and Quartz feldspar porphyry (QFP) dykes.

Nyankanga rock mass is categorized as a good rock made up of hard rock with uniaxial compressive strength (UCS) between 78 and 129 MPa, slightly rough joints spaced 0.2 to 0.42 m with joints apertures mostly less than 5 mm filled with calcite and clay material. The groundwater condition is generally moist, with water dripping in a few areas. Table 1 presents the physical and mechanical properties of the two prominent rock types in the Nyankanga Pit. Nyankanga Pit is mined by benches 10 m high on both ore and waste. The blast design on the main shot is described in Table 2.

Table 1. Nyankanga Rock Properties.

Rock type	Brazilian Tensile strength (MPa)	UCS (MPa)	Young's modulus (GPa)	Poisson's ratio	Mean sonic speed (m/s)	Rock density (t/m <sup>3</sup> )
BIF	14.2	126	90.8	0.24	4,369	2.67
DHP/DPH	15.2	110	78.2	0.25	4,683	2.62

DPH – Plagioclase rich diorite, DHP – hornblende rich diorite, BIF – banded iron formation,

Table 2. Blast design parameters.

Parameter	Unit	Symbol	Value
Hole diameter	Mm	D	203
Burden	M	B	5.5
Spacing	M	S	6.5
Bench Height	M	H	10
Sub-drilling	M	Sd	1.5
Stemming height	M	Sl	4.5

Explosive density	kg/m <sup>3</sup>	$\rho_e$	1,180
Maximum instantaneous charge	Kg	W	267
Powder factor	kg/m <sup>3</sup>	PF	0.75

The blast holes are drilled vertically in a staggered pattern and charged with a specially manufactured emulsion by ORICA; Fortis extra with properties summarized in

Table 3 [31]. The velocity of detonation (VOD) measurements were conducted during a blast using MREL's MicroTrap Data Recorder from four blast holes. The characteristics of each hole and results are presented in Table 4.

Table 3. Explosive properties.

Explosive property	Unit	Value
Density, $\rho_e$	kg/m <sup>3</sup>	1,100 – 1,250
Minimum charge diameter	Mm	64
VOD	m/s	4,100 – 6,700
Bulk Energy	MJ/kg	3.47 – 4.35 (at 1180 kg/m <sup>3</sup> )

Table 4. VOD measurements.

Pit/Lavel/Shot	Hole ID	Rock properties	Hole depth (m)	Initial density (kg/m <sup>3</sup> )	Final density (kg/m <sup>3</sup> )	VOD (m/s)
Nyankanga 8/910/ 6	KO2	Hard, less fractured	12.8	1250	1180	4401.5
Nyamulilima 1/1460/3&4	EC1	Soft rock	10	1265	1217	4694
Nyamulilima 1/1460/3&4	EC2	Transitional rock	9.8	1265	1217	5334
Nyamulilima 1/1460/3&4	EC3	Soft rock	9.4	1265	1217	4727

#### 4. Modeling a Case Study in LS-DYNA

The numerical models were created and executed using LS-DYNA Version: smp s R11.1 on a Dell Precision7810 with two Intel(R) Xeon(R) eight-core CPUs running at 2.40 GHz and equipped with 32GB RAM. Figure 3 illustrates the full-size single blast hole model established for the intact rock. The model dimensions follow the size of the blast pattern in Table 2, where the burden is 5.5 m, and the spacing is 6.5 m. The bench height is 11.5 m with a charge column of 7 m and a stemming height of 4.5 m. The radius of the blast hole is 101.5 mm, and a coupled charge is adopted where the diameter of the charge is the same as that of the blast hole. The detonation takes place 1.5 m from the bottom of the blast hole. Two free boundaries are introduced on top of the bench and along the burden, in which case the stress wave is reflected to the rock mass. Non-reflecting boundary conditions are set on the remaining sides, allowing the stress wave to transmit. The mesh size near the charge is 3 cm, and the average mesh size is 8 cm.

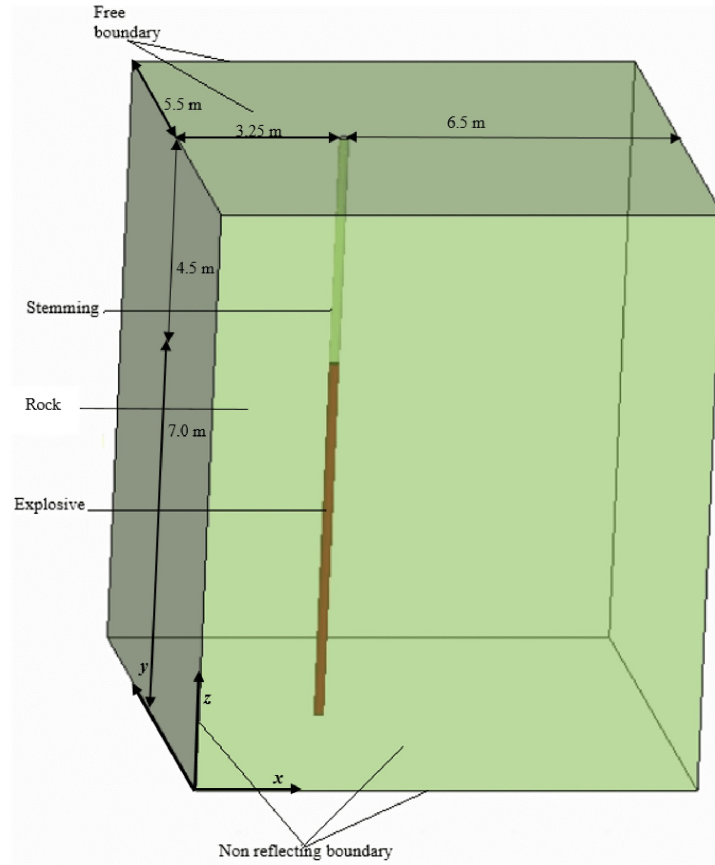


Figure 3. Numerical model of an intact rock.

For the numerical modeling, the rock mechanical properties of the Banded Iron Formation in Table 1 were calibrated to be used for analysis in the RHT model. Table 5 summarizes the calibrated properties.

Table 5. RHT model parameters for BIF.

Density (kg/m <sup>3</sup> )	Elastic shear modulus (GPa)	Unit conversion factor	Eroding plastic strain	Pore crush, B <sub>0</sub>	Pore crush, B <sub>1</sub>	Bulk Modulus (GPa)	
2670	27.03	0	2	1.22	1.22	47.06	
Failure surface constant, A	Failure surface constant, N	Compressive strength (MPa)	Relative shear strength	Relative tensile strength	Lode angle, Q0	Lode angle, *+ B	Parameter for polynomial EOS, T <sub>2</sub> (GPa)
1.6	0.6	126	0.18	0.11	0.68	0.1015	0
Ref. compressive strain rate (s <sup>-1</sup> )	Ref. Tensile strain rate (s <sup>-1</sup> )	Break compressive strain rate (s <sup>-1</sup> )	Break tensile strain rate (s <sup>-1</sup> )	Compressive strain rate exponent, β <sub>c</sub>	Tensile strain rate exponent, β <sub>t</sub>	Pressure influence on plastic flow	
0.00003	0.00003	3E+25	3E+25	0.026	0.007	0.001	
Compressive yield surface parameter	Compressive yield surface parameter,	Shear modulus reduction factor	Damage parameter, D <sub>1</sub>	Damage parameter, D <sub>2</sub>	Minimum damage residual strain	Residual surface parameter, AF	Residual surface parameter, NF
0.53	0.7	0.5	0.04	1	0.015	0.61	1.6
Gruneisen gamma	A <sub>1</sub> (GPa)	A <sub>2</sub> (GPa)	A <sub>3</sub> (GPa)	P <sub>crush</sub> (MPa)	P <sub>comp</sub> (GPa)	Porosity exponent	Initial porosity
0	32.5	37.8	9.5	125	6	3	1

The explosive column was modeled using an Eulerian grid. The high explosive burn material and Jones-Wilkins-Lee (JWL) EOS are used to model explosive charge detonation. The JWL equation of state is a high-energy combustion model that can reliably predict higher explosion pressures. The model defines the pressure of detonation products  $P_{cj}$  using equation (8) [32].

$$P_{cj} = A \left( 1 - \frac{\omega}{R_1 v} \right) e^{-R_1 v} + B \left( 1 - \frac{\omega}{R_2 v} \right) e^{-R_2 v} + \frac{\omega E}{v} \quad (8)$$

Where  $A$ ,  $B$ ,  $R_1$ , and  $R_2$  and  $\omega$  are material constants,  $E$  is detonation energy per unit volume, and  $v$  is the relative specific volume of detonation products. The input parameters for the JWL Model for Fortis Extra properties are adapted from the similar emulsion explosive E682 calibrated by Hansson [33] in Table 6.

Table 6. E682 explosive parameters.

Explosive Type	Density (kg/m <sup>3</sup> )	VOD (m/s)	$P_{cj}$ (GPa)	$A$ (GPa)	$B$ (GPa)	$R_1$	$R_2$	$\omega$	$E_o$ (GPa)	$v_o$
E682	1,180	5,211	9.53	276.2	8.44	5.2	2.1	0.5	3.87	0

Rock masses are made up of intact rock and discontinuities such as joints, faults, and bedding planes. Such discontinuities, usually weaker than the intact rock, affect rock masses' response to blast loadings. The joint parameters such as the joint width, infill material, orientation, persistence, spacing, and distribution pattern significantly impact the propagation of blast waves and hence rock mass fracturing. The numerical model analyzed two types of joints to determine the impact of parameters: joints without filling material and joints filled with soft rock. Air in the empty joint was modeled as NULL material and ALE part with properties described in Table 7, while soft rock infill was modeled using the plastic kinematic material model as a Lagrangian part with properties defined in Table 8.

Table 7. Parameters for Air

Density (kg/m <sup>3</sup> )	C4	C5	C6	Eo (MPa)	Vo
1.29	0.4	0.4	0	0.5	1

Table 8: Soft rock parameters

Density (kg/m <sup>3</sup> )	Young's Modulus (GPa)	Poisson's ratio	Yield stress, (MPa)	Tangent Modulus, (GPa)	Hardening parameter	Failure strain, FS
1,160	5	0.35	0.4	4	0	0.5

## 5. Results and Discussion of Simulation Results

### 5.1 Damage Zones Estimation on the Intact Rock

The theory of rock fracture and fragmentation due to blasting suggests an overall combined damage mechanism. The intensity, propagation, and interaction of shock waves (stress waves) are responsible for initially fracturing the rock (conditioning), and the ensuing gas pressure predominantly affects fragmentation breakage and displacement beyond the immediate blast hole region. The detonation pressure from the commercial explosives, usually higher than 10 GPa, induces high shock waves on the blast hole wall way ahead of expanding gases (the gas pressure), causing the borehole's initial pulverized zone. The shock wave quickly decays into a high amplitude stress wave traveling at longitudinal wave speed in the rock mass, forming the fractured and incipient cracked zones. When encountering a free surface, these waves are reflected, causing spalling if its intensity exceeds the rock's tensile strength. Further extension and propagation of cracks are caused by penetrating gases. From the study conducted by Hustrulid [34] using ANFO in medium-strength rock, the crushed zone can extend up to 6 times the hole diameter, the fracture zone up to 20, and the influenced zone up to 60 times the hole diameter.

The blasting process was modeled for a 3D intact rock described in Section 4. The estimate of damage zones is based on the damage contours on the x-y plane 2 m from the bottom of the bench, where the crushed zone is represented by the circular red contour around the charge; the fractured zone is represented by the cracks propagating from the crushed zone. Spalling occurs at the free face propagating inwards towards the blast hole, causing further fracturing, as seen in Figure 4. The blast hole expands due to gas expansion from a radius of 101.5 mm to 163.2 cm. The rock around the blast hole is completely pulverized, forming a crushed zone of 250 mm at 0.8 ms, which is 2.5 times the blast hole radius. The damage decreases with increased distance, with the pattern crossing near the blast hole and extending radially away from the blast hole, forming a fractured zone extending to 5 m in all directions at 2.5 ms.

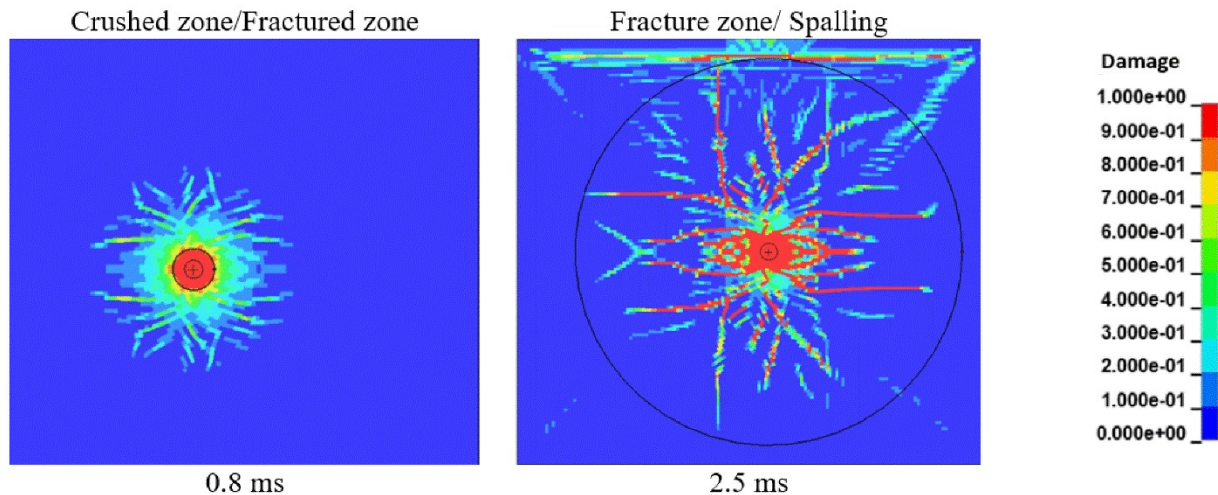


Figure 4. Damage zones around the blast hole.

The pressure at the end of the crushed zone is 949 MPa, and the PPV is 124 m/s. Dotto et al. [35] conducted a study to estimate the damage zones around the charge from the same case study, and they compared several approaches. Table 9 summarizes the result of their study. From the numerical model, the pressure at 161 mm is 1330 MPa, close to the predicted value of 1488 MPa; the PPV at 161 mm is 180 m/s. The numerical model results suggest that the wave still has the crushing capacity until it reaches 949 MPa, which is close to the pressure estimated using the Hugoniot elastic limit approach in Dotto et al. [35] study. In the previous study by Dotto et al. [35], the fractured zone was obtained to extend to 5.4 m at 1.21 m/s PPV. From the numerical model, the fractured zone at 2.5 ms has extended to 5 m, where the maximum PPV and the peak pressure are 6.2 m/s and 48 MPa, respectively. At 5.4 m, the maximum pressure is 40.8 MPa, and the PPV is 1.2 m/s, the same value obtained in the previous study.

Table 9. Crushed zone parameters [35].

Approach	Crushed zone radius (rc; mm)	Pressure at the limit of the crushed zone (Pe; MPa)	PPV at the limit of the crushed zone (m/s)
Study approach	161	1,488.13	77.9
Shock wave transfer	185	1,683.94	105.25
Hugoniot elastic limit	164	912.15	80.47
Far-field monitoring	161	510.79	54.32

## 5.2 The Influence of Joints Parameters

The influence of joint properties and parameters on blast-induced fragmentation has been studied by several researchers for various applications [18, 19, 36-38]. Each study concluded that the presence of joints affects blast outcomes and is worth investigating for effective blast design. In this study, several properties are investigated with their influence on blast energy distribution and crack propagation.

### 5.2.1. Joint Filling Material

When a stress wave encounters a joint, partial to complete wave reflection may occur depending on the joint properties. The effects of joints infill material were analyzed through simulations of empty joints and joints filled with soft rock. Table 6 and Table 7 define material properties utilized for this purpose. The intact rock is used as the base case. Three horizontal joints were modeled 1.8 m from the bottom of the bench; each joint is 3 cm wide and spaced 0.42 m. The simulation models were run for 2 ms. Figure 5 shows the pressure (a-1, a-2, and a-3) and the damage contours (b-1, b-2, and b-3). During the simulation, the pressure was monitored 1 m away from the blast hole at four locations marked A, B, C, and D. Figure 5(a) shows the locations.

Figure 5(a-1, a-2, and a-3) illustrates that the stress wave energy is affected by the presence of joints, and the effect depends on the joint filling material. In this case, the effect is more pronounced on empty joints than on the joints filled with soft rock. The resulting damage is presented in Figure 5 (b-1, b-2, and b-3) for the three cases where a clear distinction of damage progression in regions separated by the joints is observed. With the stress wave reflected on each joint, an upper section has a narrower damage zone compared with the preceding section with a clear boundary at the rock/joint interface, in this case, the empty joints have more variable damage zones.

Figure 6 (a, b, and c) shows the peak pressure variations at the four locations (A, B, C, and D). In the intact rock, the peak pressure in all locations is relatively uniform. In the jointed rock mass, the peak pressure increases significantly between the joints, with a higher effect between empty joints. In the soft rock, the pressure increase is consistent after every joint due to partial wave reflection at the joint and the increase in the joint's stiffness increasing its transmission capacity. The highest pressure between joints is observed with empty joints at locations B and C, where more energy is reflected at the joints. The damage at such locations, however, is less than what is observed in the intact rock and soft rock joints due to higher confinement which requires way higher energy for the fracture to occur. At location D, where no more joints are encountered, the peak pressure is almost the same as the intact rock.

Figure 7 shows that beyond the joints nearly 2 m away, for the jointed rock mass, the peak pressure drops to the average of 150 MPa, close to the peak pressure encountered by the intact rock. For the four monitoring points, the peak pressures in the intact rock are achieved between 0.28 and 0.44 ms; for the joints with soft rock filling, the peak pressure happens between 0.28 and 0.48 ms, and with empty joints between 0.28 and 0.52 ms demonstrating that with variable joint infills, the stress wave speed varies too.

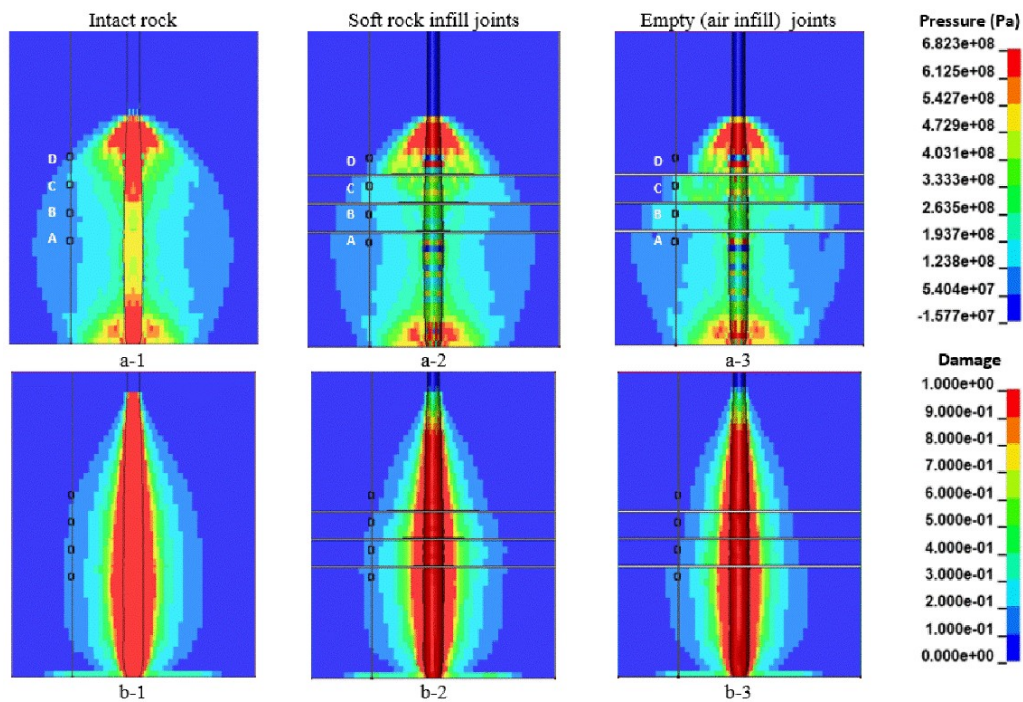


Figure 5. Stress wave propagation and damage in variable joint properties.

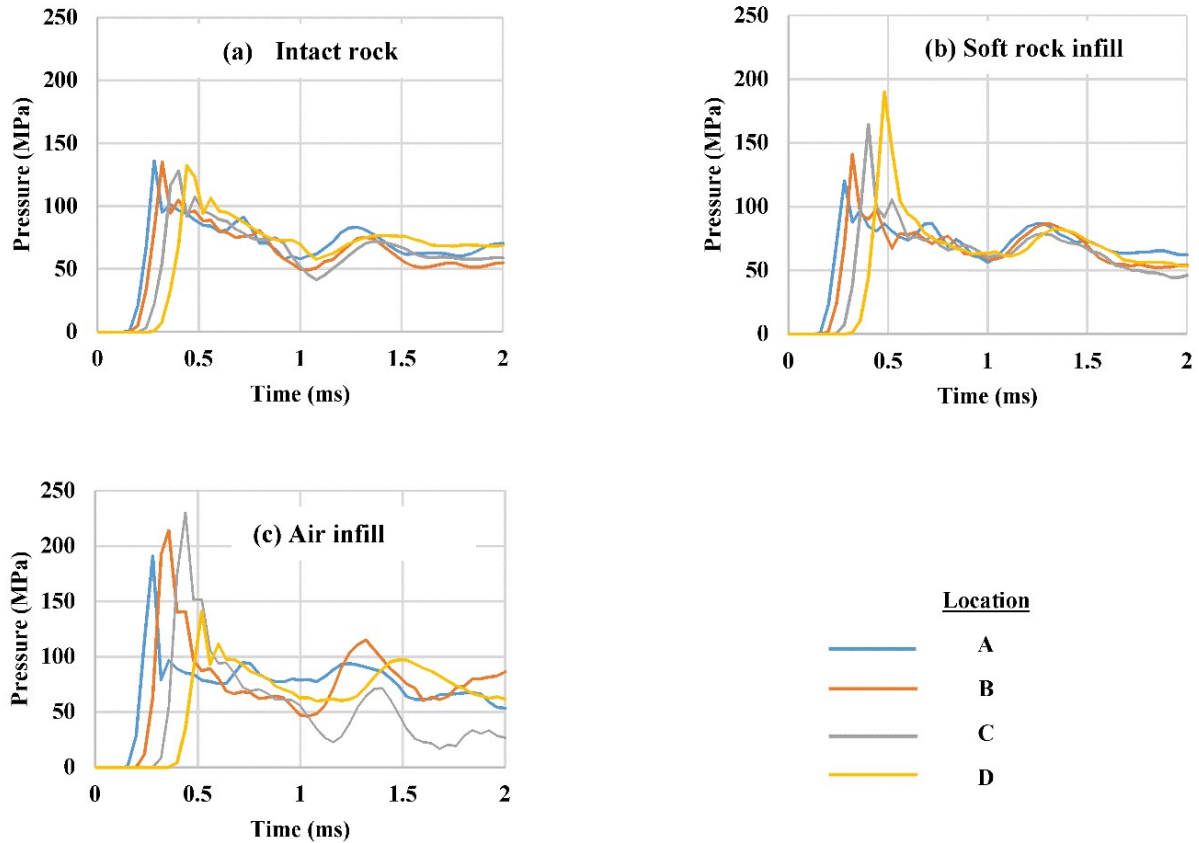


Figure 6. Pressure plots for horizontal joints.

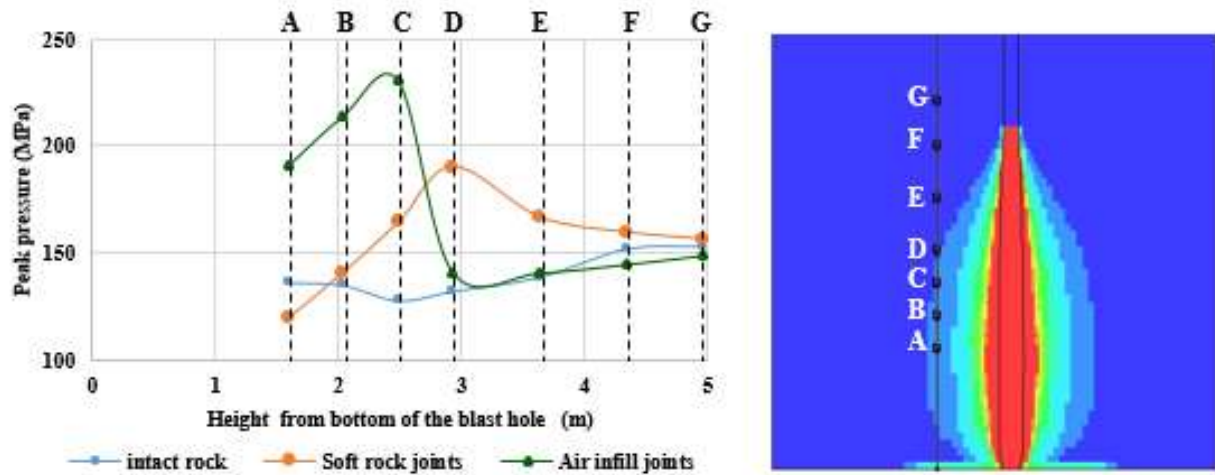


Figure 7. Peak pressure variation with distance from the bottom of the blast hole.

When similar joints, 10 cm wide, were placed 0.5 m from the blast hole, reflection at the joint/rock boundary is observed with more effect on air-infill joints, as shown by pressure contours at 0.7 ms in Figure 8. Such occurrence leads to a bigger crushed zone forming around the charge on the incident side of an empty joint and less fracturing beyond, as illustrated by Figure 9. For the air-infill joints, a pressure-neutral part is also observed between the joint and blast hole due to collision between the reflected wave and the wave front. The peak pressure was monitored at 0.5 m intervals from the blast hole. Figure 10 illustrates the relationship between pressure and distance for the two joint filling materials. With an empty joint, higher pressure near the blast hole (at 0.5 m distance) is from wave

reflection and higher compressibility at the joint. The pressure drops drastically and falls below the pressure through soft rock at a 1.5 m distance from the blast hole.

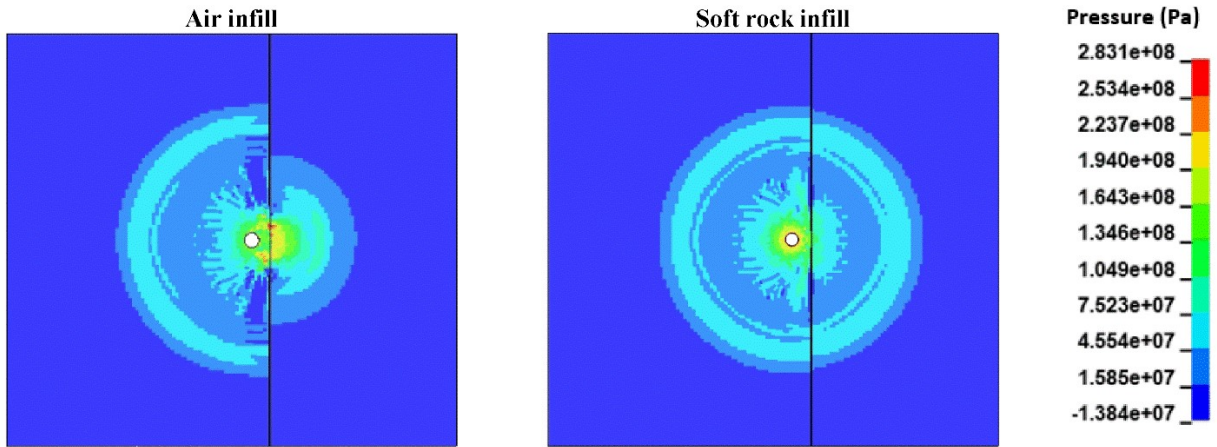


Figure 8. Pressure attenuation along different joints infill properties at 0.7 ms.

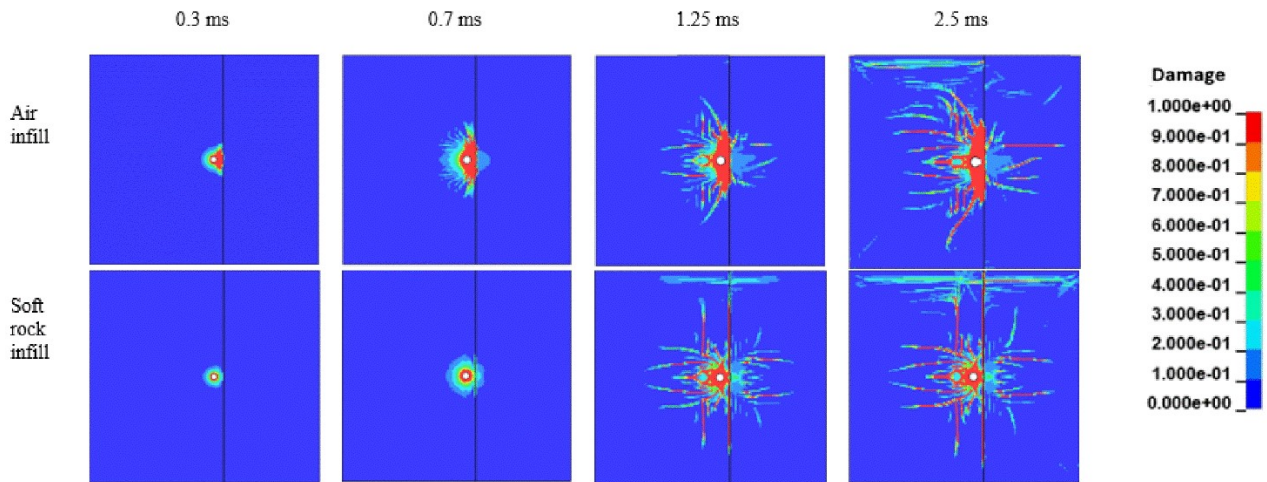


Figure 9. Damage beyond different joints' material.

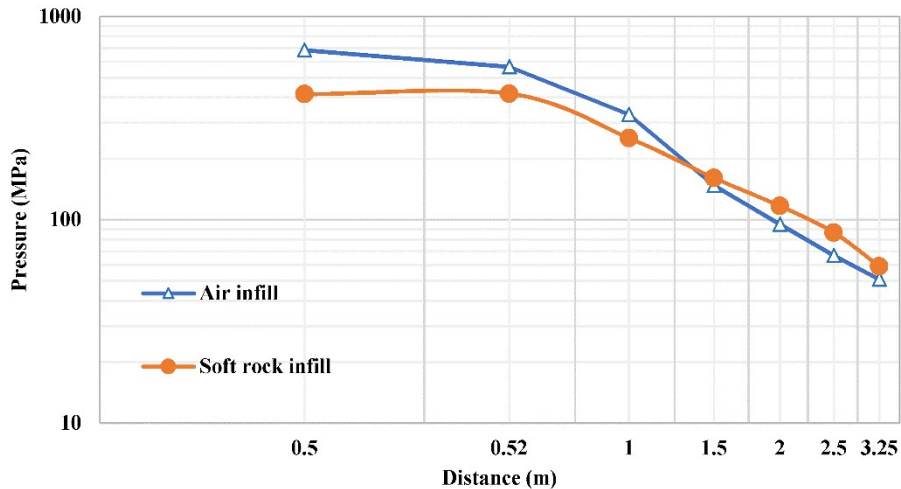


Figure 10. Pressure propagation in different joint materials.

### 5.2.2. Joint Width

Two scenarios analyzed the effects of joint size in blast wave propagation with joints 3 cm and 10 cm wide on a 2D model. In both cases, the joints are perpendicular to the burden and are placed 1 m from the charge. Figure 11 shows the influence of the joint width on crack propagation captured at 2.5 ms. With a wider joint, the extent of damage indicates that the rock on the opposite side of the joint is experiencing less fracturing. When the stress wave reaches the joint interface, the stiffness of the joint increases at a rate that depends on the thickness of the joint and the normal stress. For the same infill material and normal stress, smaller joints have higher specific stiffness growth than wider joints. An increase in joint stiffness increases the joint's transmission coefficient. Figure 12 describes the pressure history for both cases from the rock/joint interface before and after and within the joint. The two peak values are observed on the pressure plots before the joint from the wave front and the reflection at the joint. The pressure in the joint is higher than the incident pressure in both cases, a higher peak is observed in the narrow joint. The transmitted stress wave on a wider joint is lower due to filling material deformation under the stress wave, which is also seen at the rock/joint interface in Figure 11, causing energy absorption and a decrease in the energy transfer capacity of the joint.

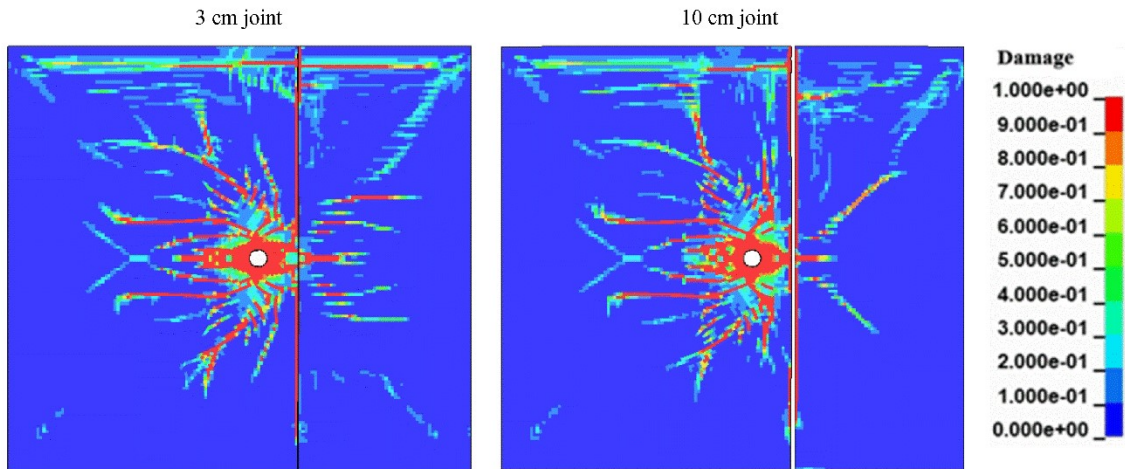


Figure 11. Joint width effects on crack propagation.

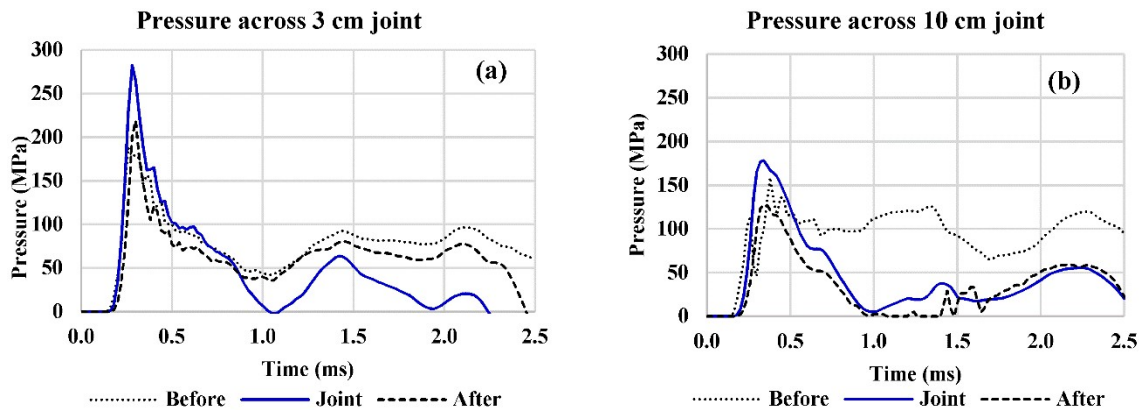


Figure 12. Pressure across joint width.

### 5.2.3. Joint Distance from the Blast Hole

Four scenarios with the joint placed at 0.5 m, 1 m, 2 m, and 3.25 m from the blast hole were analyzed for the effect of joint distance on stress wave and crack propagation from a 2D model. The joint infill

material is a soft rock. The results are summarized in Figure 13. Crack propagation beyond the joint increases as the joint distance from the blast hole increases, except for the last scenario, where the joint is 3.25 m from the blast hole. As demonstrated in Figure 14, the stress wave initially propagates outwards until it reaches the joint where it is partially blocked and reflected as a tensile wave causing more cracking/crushing on the incident side. Pressure build-up occurs inside the joint due to an increase in the joint's stiffness. Since the infill material is weak, deformation occurs inside the joint absorbing some of the stress wave energy. Such deformation transmits to the rock around the joint as seen in Figure 13. This effect decreases with the increase in the joint distance. Wave transmission through the joint depends on the wave strength and the extent of deformation within the joint.

At 0.5 m joint distance, most of the wave energy is reflected and used up on joint deformation, causing less fracturing on the other side. Wave energy reflection and joint deformation decrease with distance increase hence better wave transmission across the joint and increasing crack propagation on the opposite side as seen in 1 m and 2 m joint distance scenarios. At 3.25 m, the stress wave has attenuated a lot, way less deformation occurs in and around the joint, less stress wave is transmitted across the joint, and therefore less cracking on the opposite side of the joint.

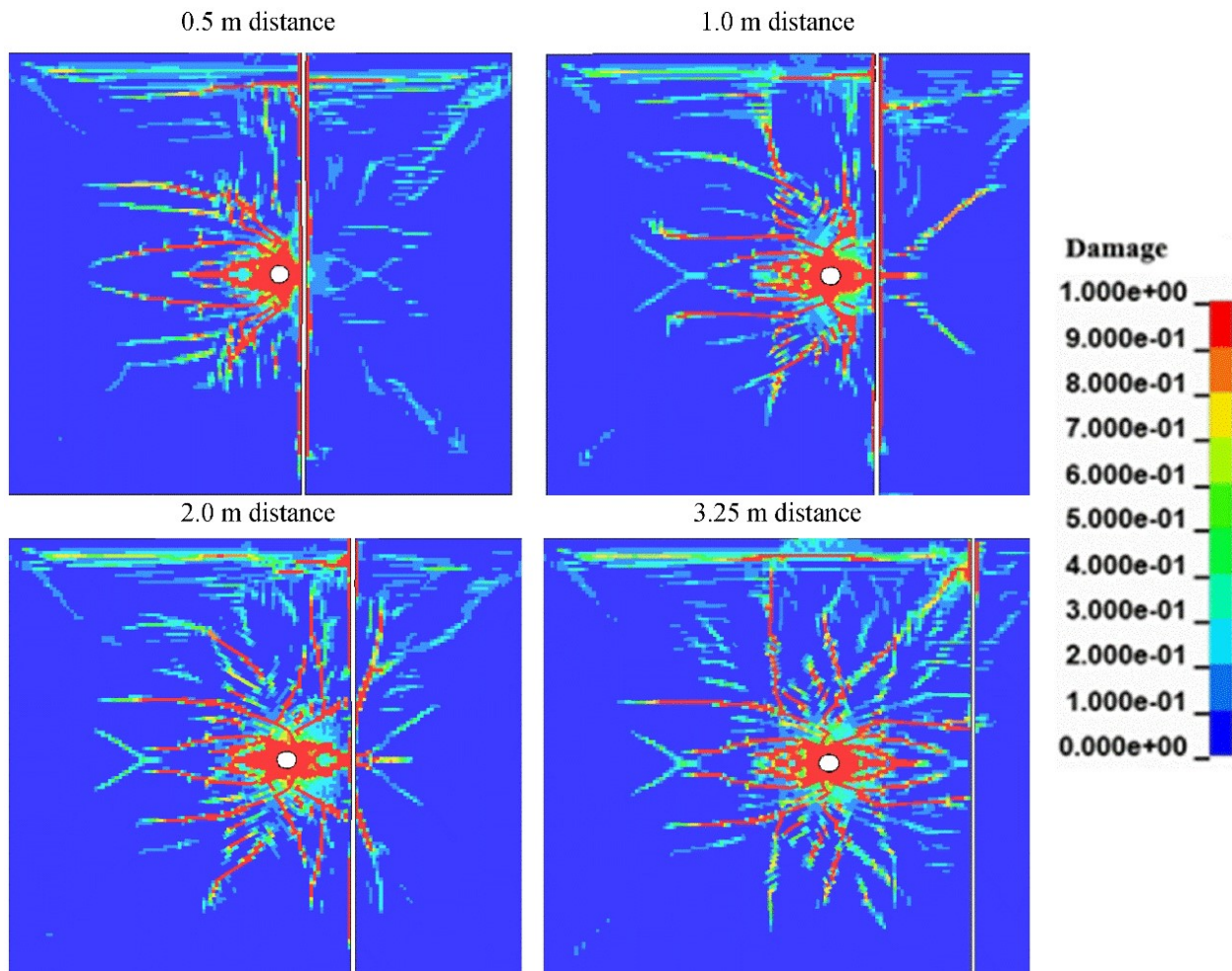


Figure 13. Damage distribution in variable joints distance.

#### 5.2.4. Joints Spacing

Three scenarios were investigated for variable joint frequency, which are 2, 3, and 4 joints per meter. The simulation results show that the increase in joints frequency reduces the burden cracking

significantly. Figure 15 illustrates the effect of joint frequency on wave and crack propagation. With an increase in joint frequency, the wave goes through multiple partial reflections and transmissions, weakening the wave strength. Similarly, joint deformation consumes some wave energy, and with the increase in joint frequency, this occurs multiple times contributing to weakening the stress wave. This results in less fractures on the opposite side of the joints.

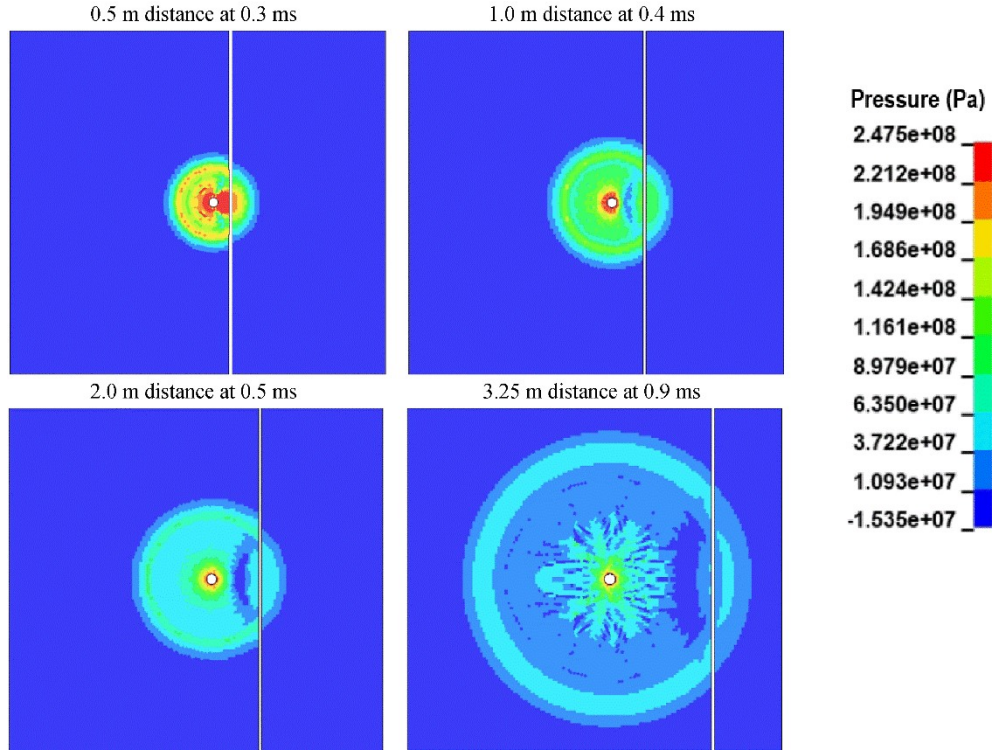


Figure 14. Stress propagation in variable joint distances.

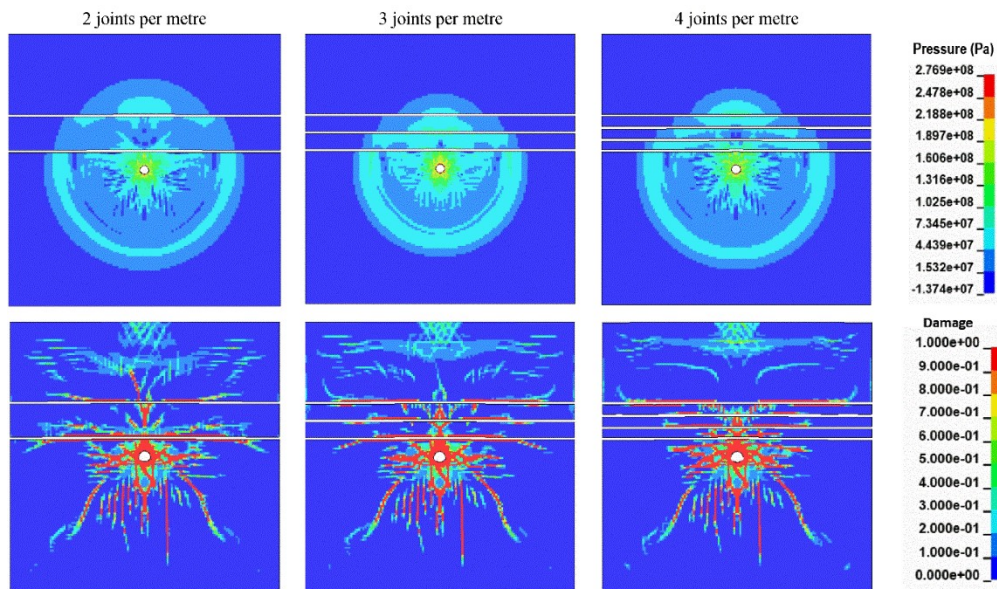


Figure 15. Joints frequency.

### 5.2.5. Joints Orientation

Five models of different joint orientations, including joints at 15, 30, 45, 60, and 90 to the free face, were analyzed to investigate the effects of joint orientation on blast wave propagation and rock mass fragmentation. The joints are 3 cm wide, with soft rock as the infill material. The general view of the models and the damage distribution at 2.5 ms for variable joint orientations and the intact rock as a baseline is illustrated in Figure 16. The orientation of the joints influences the direction and propagation of cracks. Cracks propagation beyond the joint depends on the angle at which the stress wave hits the joints. Compared with the intact rock, near horizontal angles, i.e., 15 and 30 degrees, the joints are hit perpendicular to the joint, energy gets transmitted, and cracks propagate beyond the joint. Transmission decreases with the increase in the joint orientation, as seen with 60- and 90-degree joints. Since the joints' orientations do not favor further cracking from wave reflection at the free face, the burden cracking is reduced significantly.

### 5.2.6. Parallel Versus Random Joint Sets

A model with a free face on the top of the bench and the two opposite sides of the blast hole was used to analyze the effect of joint sets' orientations on the blast wave propagation and rock fracturing for parallel and random joints. On the opposite sides, free faces were used to ensure the two scenarios' fair comparison. In both scenarios, three (3) joints are placed within 2 to 4 m of the blast hole. When the wave encounters a joint set, multiple reflections and partial transmissions occur at the joints' interfaces. With intersected/random joints, the direction of transmitted and reflected waves is changed, adding to the attenuations caused by the joints' properties. Figure 17 (a) describes the pressure contours at 1 ms, and Figure 17 (b) the damage at 2.5 ms for parallel and random joint orientations. The burden breakage is better with parallel joints case due to less attenuation across the joints as shown in Figure 18.

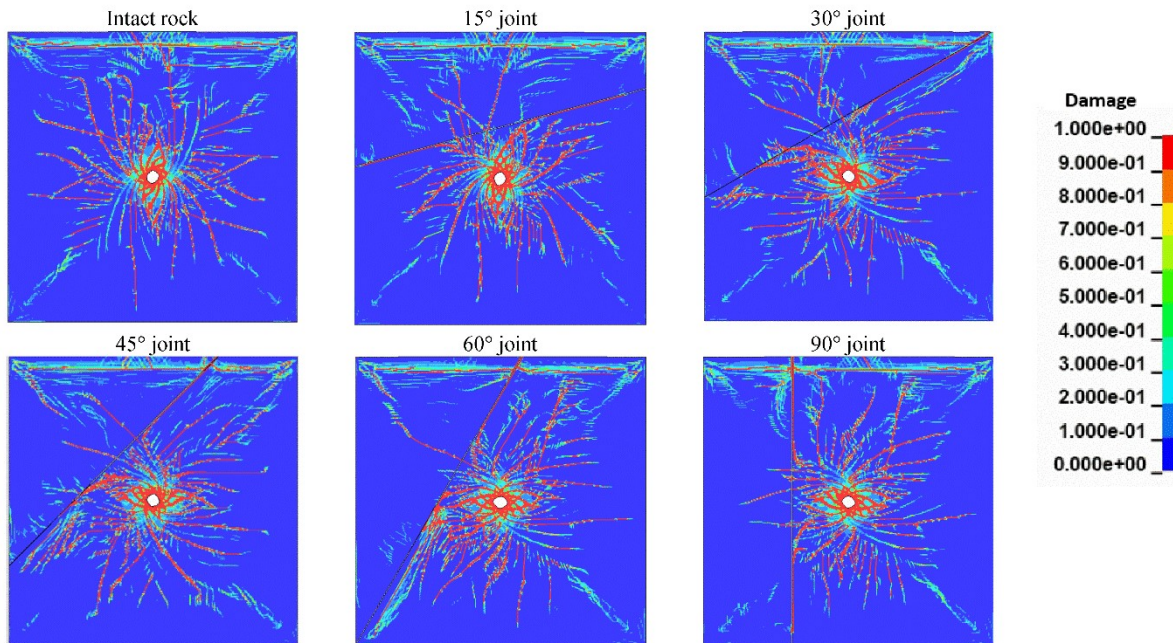


Figure 16. Damage distribution from joints orientation.

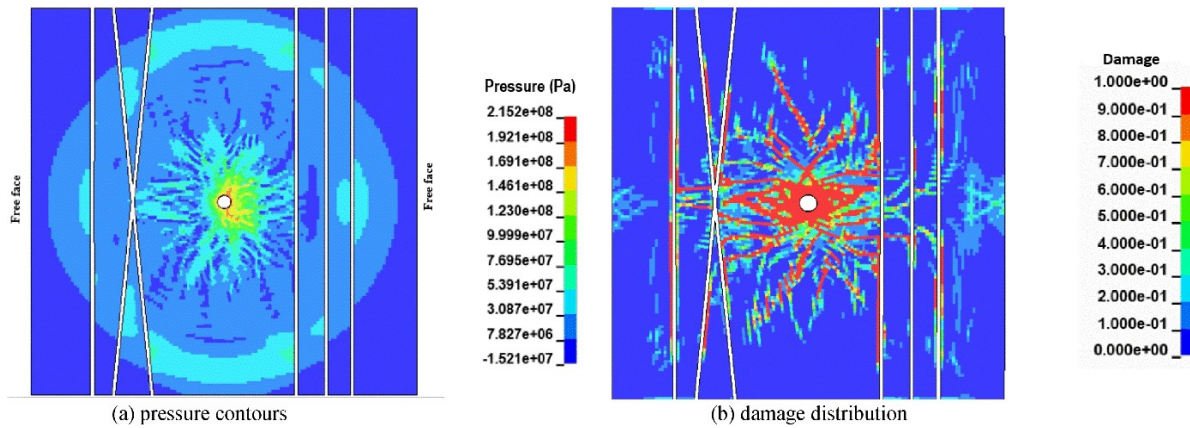


Figure 17. Random joint sets analysis.

### 5.3 Initiation Delay

The stress wave intensity and the interaction from neighboring charges control rock fragmentation around the blast hole. The effect of initiation timing is investigated from two blast holes with one joint 1.5 m from the first blast hole. Two scenarios are run, the first being both charges detonated at the same time and the second with a 1 ms delay on the second blast hole. The simulation is run for 2 ms from the detonation of the second blast hole; therefore 2 ms and 3 ms for the first and the second scenarios, respectively. The results in Figure 19 reveal that the delay is important in enhancing fragmentation by allowing enough time for the cracks to grow especially beyond the joint. It is important to determine the optimum delay, which is the function of the rise and duration of the stress pulse, the stress wave speed, and crack propagation in the rock mass, [39].

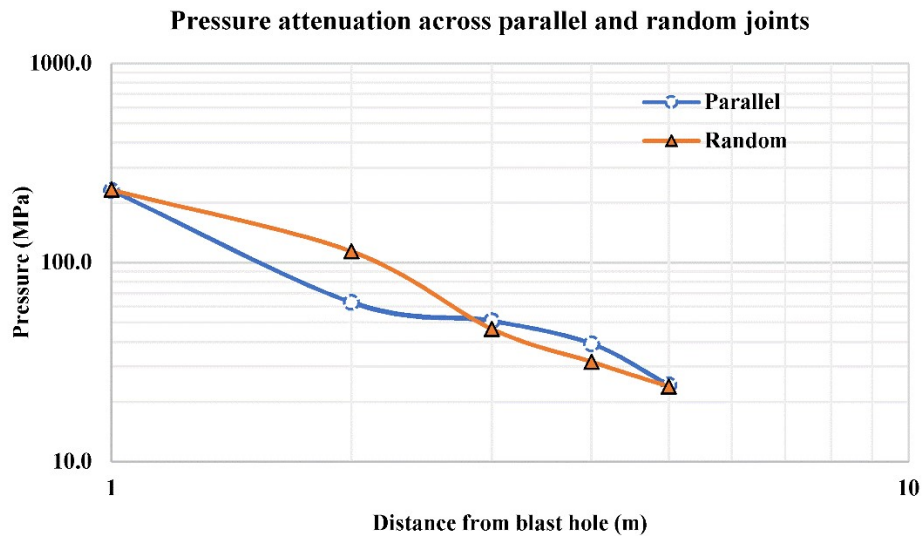


Figure 18. Pressure attenuation across joint sets.

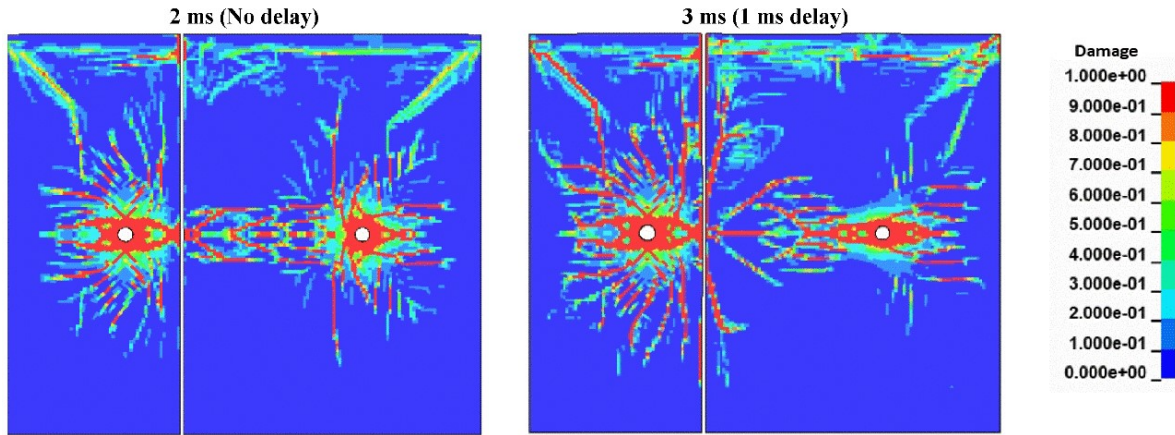


Figure 19. Blast-induced damage from detonation timing.

### 5.4 Rock Properties

During the blasting process, wave propagation and crack propagation are greatly influenced by the rock's physical and mechanical properties. Two models are investigated for the effects of rock strength on the propagation of stress waves and the formation of damage zones around the charge. hard rock.

Table 10 shows the properties of the weaker rock. Figure 20(a) shows that the stress waves propagate faster in the hard rock than in the soft rock. Damage zones in Figure 20(b) are clearly defined on the hard rock; on the soft rock, on the other hand, due to less resistance offered by the rock strength, the crushed zone is not formed around the charge nor the distinctive cracks around the charge, instead the damage is defined by the separation between individual elements of the model. Figure 21 illustrates that pressure attenuates faster in soft rock than in hard rock.

Table 10. Soft rock properties.

Density (kg/m <sup>3</sup> )	Compressive strength (MPa)	Tensile strength (MPa)	Young's modulus (GPa)	Poisson ratio	Elastic shear modulus (GPa)
1600	10	1	25	0.3	9.8

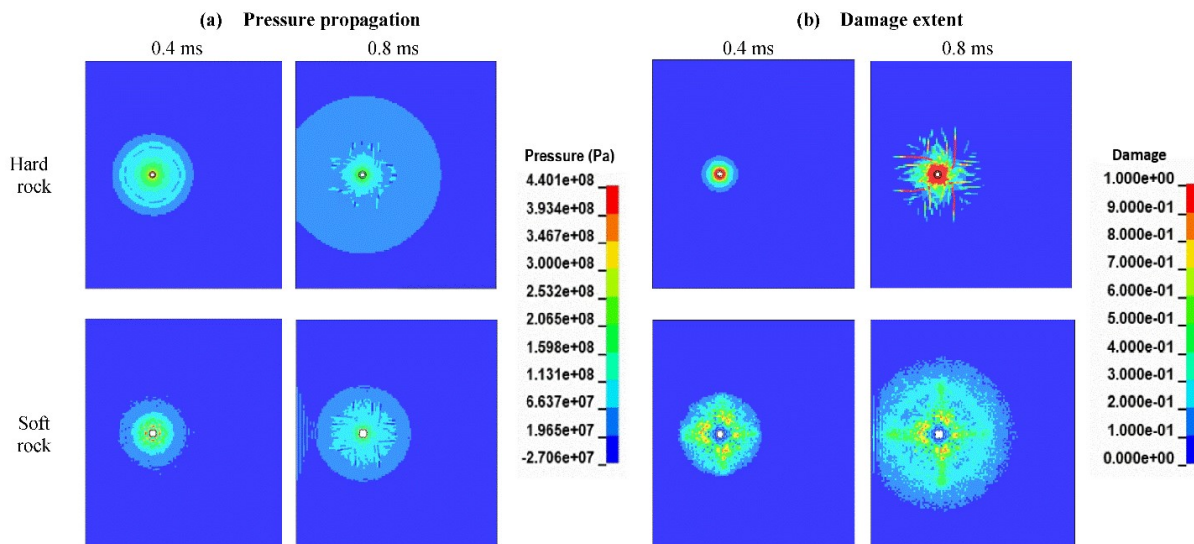


Figure 20. Pressure and damage propagation in hard and soft rock.

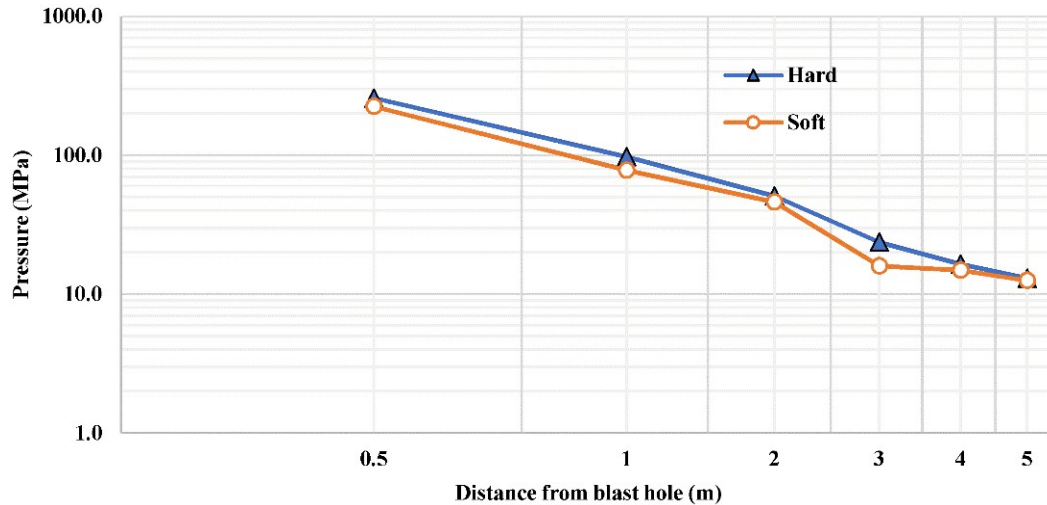


Figure 21. Pressure attenuation in hard and soft rock.

## 6. Field Blast Fragmentation

This section presents the outcomes of the filed blast for the same data used in the simulation. Data for rock mass properties, blast design, and explosive properties for the case study are discussed in Section 2. Figure 22 shows the lithologies and joint orientations mapped on the pit wall on locations P1, P3, P5, P7, P9, P11, and P13 and projected into the bench. Blast monitoring and fragmentation analysis for the blast shot was performed using Wip-frag software [40] from the images taken on top of the blasted muckpile at locations P2, P4, P6, P8, P10, P12, and P14 (Figure 22). Please refer to Dotto et al. [35] for a complete analysis of the results. Figure 23 shows the relationship between the fragmentation size (P50) and the distance between the blast hole to the monitoring point.

In the case of isotropic and homogeneous rock mass, the fragmentation size increases with the increase in distance from the blast hole. Based on the analysis of fragmentation, P8 has the smallest fragmentation size and is the closest to the blast hole. Although multiple random joints are crossing the burden, the monitoring location is very close to the blast hole (within 0.8 m), within the high-intensity stress wave zone, resulting in good fragmentation. P6 is the furthest from the blast hole and has several random joints crossing the burden, leading to oversize fragmentation. P10 and P12 are almost a quarter burden from the blast hole with no joint between the blast hole and the monitoring point. A medium size fragmentation is observed in both cases since they are within the fractured zone. Although P10, which is closer to the blast hole has a bigger fragmentation (103.97mm) than P12 (87.98 mm), it has a higher size reduction factor (22) as compared to P12 (16), which is the ratio of the average intact block size to the average fragmentation size.

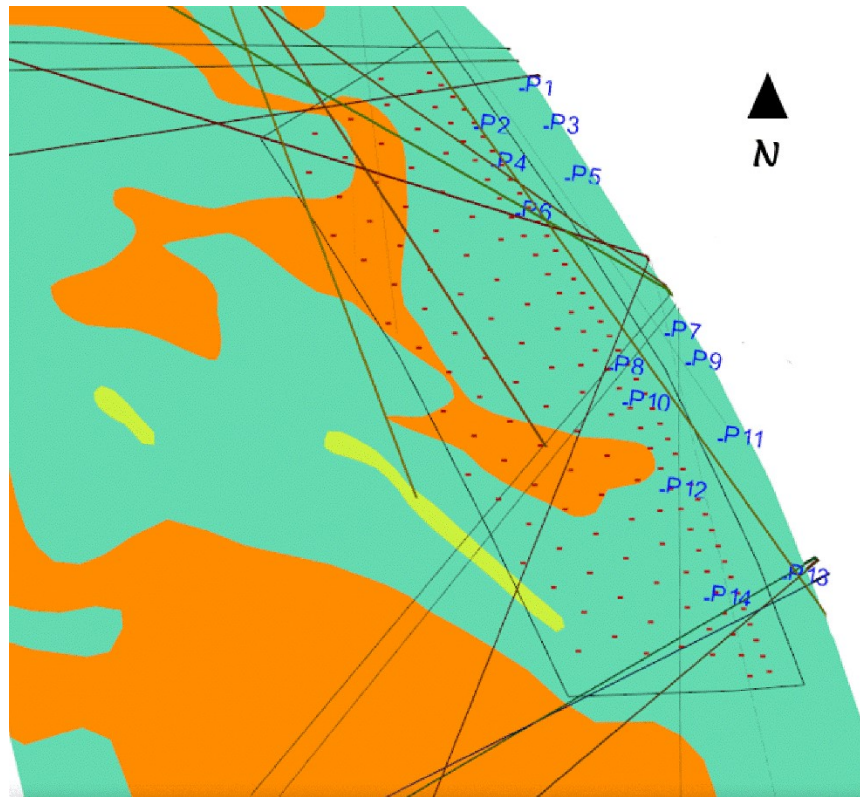


Figure 22. Mapped structures on the pit wall.

Muckpile Point	Distance from blast hole (m)	Intact block size (mm)	Frag. size P <sub>50</sub> (mm)
P8	0.8	670	73.67
P6	2.8	2,380	267.09
P10	1.27	2,260	103.97
P12	1.65	1,420	87.98
P14	1.99	1,300	184.40

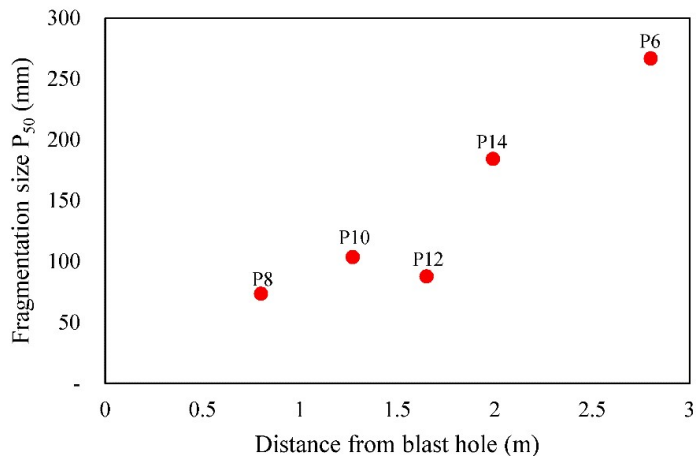


Figure 23. Fragmentation along the burden.

## 7. Discussion

The simulation results show that several factors influence the fracturing process by blasting. The formation of damage zones around the charge depends on explosive strength and detonation efficiency which determine the energy output, and the rock mass strength and structural properties which control fracturing and energy transmission. In soft rock, distinct damage zones are not formed due to less confinement from a weaker material. Instead, damage occurs through the separation of individual elements in the model. This has also been observed in the study conducted by Cui et al. [41]. For the hard rock, the analytical models using the field data underestimate the size of the crushed zone. For the same rock strength, the simulation results show that the wave still has a

crushing capacity at 1488 MPa until it reaches 949 MPa. Both field results and simulation results show that the fracture zone for the intact rock can extend to 5.4 m where the pressure is 40 MPa, and the PPV is 1.2 m/s. Beyond that, the damage caused is not significant in rock fragmentation.

Joint parameters such as filling material, joint width, joint distance from the charge, fracture frequency, and joints/joint sets orientations affect the distribution of blast energy and therefore impact the blast-induced fragmentation. Results from the simulation model are similar to the field blast, both indicating that, for the same amount of blast energy, the burden fracturing depends on the distance from the blast hole, the structures present, and their properties.

Interaction between charges plays a major role in blast outcomes. Simultaneous detonation hinders crack propagation by increasing confinement between the charges. Initiation delay between adjacent holes is important in minimizing the interference of the stress wave and allowing time for cracks to form. Delays are also important in pre-conditioning the rock at a distance from the charge with micro-cracks that can be extended by the gas pressure or the next charge, improving fragmentation.

Generally, efficient fracturing in jointed rock mass requires understanding the rock mass's physical and mechanical properties, the influence of joint parameters, and the design modifications necessary to improve the outcomes. Design modifications can include burden and spacing adjustments, changes in the type of explosive to ensure fracturing efficiency depending on the encountered rock mass, or techniques to vary explosive quantity per volume blasted to ensure effective distribution of explosive energy.

## 8. Conclusion and Future Work

Variable rock mass properties impact the distribution of explosive energy and blast outcomes. Several methodologies have been used to understand the interaction between the rock mass and explosive energy and predict the blast outcomes. This study used finite element numerical modeling using the RHT model in LS-DYNA to simulate the effect of rock properties, joint parameters, and initiation delay on the distribution of explosive energy and the fracturing process.

The simulation outcomes were compared to the results obtained from the field blast. Joint parameters such as the filling material, joint width, joint distance from the charge, fracture frequency, and individual joints and joint sets orientations were modeled, and outcomes were compared with the field blasts. The results showed that when the RHT model parameters are calibrated based on real data, they can be used to simulate the fragmentation process, as confirmed by the similarities between the simulation's damage plots and the distribution measured in the field.

The three-dimensional simulation of blast-induced damage on intact rock showed that the damage begins with forming a crushed zone around the charge, which propagates outwards, preferably towards the free surface. The reflection of the stress wave from the free surface causes spalling at the free face progressing towards the blast hole if the stress wave exceeds the rock's tensile strength. Less fracturing is evident on non-reflecting boundaries. In the case of jointed rock mass, the formation and shape of damage zones vary significantly depending on the properties of discontinuities.

This work can be extended by coupling LS-DYNA with other software to measure and estimate the fragmentation size from the damage plots to be able to compare with the field-blasted muckpile fragmentation. One of the major focuses in mining blasts is to attain the pit design. This study can be extended to assess the impact of the rock mass properties on the final pit wall and pit floor and check for over-breaks and under-breaks.

## 9. References

- [1] Liu Q, Katsabanis PD. A Theoretical Approach to the Stress Waves Around a Borehole and Their Effect on Rock Crushing. Proceedings of the Fourth International Symposium on Rock Fragmentation by Blasting-Fragblast-4; Vienna, Austria1993. p. 9-16.
- [2] Esen S, Onederra I, Bilgin HA. (2003). Modelling the size of the crushed zone around a blasthole. *International Journal of Rock Mechanics and Mining Sciences*, 40(4), 485-95. doi:[https://doi.org/10.1016/S1365-1609\(03\)00018-2](https://doi.org/10.1016/S1365-1609(03)00018-2)
- [3] Grady DE, Kipp ME. (1980). Continuum modelling of explosive fracture in oil shale. *International Journal of Rock Mechanics and Mining Sciences & Geomechanics Abstracts*, 17(3), 147-57. doi:[https://doi.org/10.1016/0148-9062\(80\)91361-3](https://doi.org/10.1016/0148-9062(80)91361-3)
- [4] Zhu Z, Mohanty B, Xie H. (2007). Numerical investigation of blasting-induced crack initiation and propagation in rocks. *International Journal of Rock Mechanics and Mining Sciences*, 44(3), 412-24. doi:<https://doi.org/10.1016/j.ijrmms.2006.09.002>
- [5] Yoon J, Jeon S, editors. Use of a modified particle-based method in simulating blast-induced rock fracture. Proceedings of the 9th International Symposium on Rock Fragmentation by Blasting, Fragblast; 2010.
- [6] Onederra IA, Furtney JK, Sellers E, Iverson S. (2013). Modelling blast induced damage from a fully coupled explosive charge. *International Journal of Rock Mechanics and Mining Sciences*, 58, 73-84. doi:<https://doi.org/10.1016/j.ijrmms.2012.10.004>
- [7] Fleetwood K, Villaescusa E, Li J, editors. Limitations of using PPV damage models to predict rock mass damage. Thirty-Fifth Annual Conference on Explosives and Blasting Technique; 2009; Denver, CO, USA: International Society of Explosives Engineers.
- [8] Persson PA, Holmberg R, Lee J. Rock blasting and explosives engineering: CRC Press; 1994.
- [9] Sun C. Damage zone prediction for rock blasting. Salt Lake City, UT, USA: University of Utah; 2013.
- [10] Junkin W, Ben-Awuah E. (2023). Determining characteristic fractured volumes in DFN models using fracture intensity variability analysis. *GEM - International Journal on Geomathematics*, 14(1), 17. doi:10.1007/s13137-023-00226-9
- [11] Zhang ZX. Rock Fracture and Blasting: Theory and Applications Amsterdam: Elsevier; 2016.
- [12] Azadmehr A, Jalali SME, Pourrahimian Y. (2019). An Application of Rock Engineering System for Assessment of the Rock Mass Fragmentation: A Hybrid Approach and Case Study. *Rock Mechanics and Rock Engineering*, 52(11), 4403-19. doi:10.1007/s00603-019-01848-y
- [13] Lizotte Y, Scoble M. (1994). Geological control over blast fragmentation. *CIM Bulletin*, 87(983), 57-71.
- [14] Yang RL, Rocque P, Katsabanis P, Bawden WF. (1994). Measurement and analysis of near-field blast vibration and damage. *Geotechnical & Geological Engineering*, 12(3), 169-82. doi:10.1007/BF00426985
- [15] Bhandari S. Changes in fragmentation processes with blasting conditions. Fragmentation by blasting. Fragblast 5. Quebec, Canada: A. A. Balkema; 1996. p. 301-9.
- [16] Mortazavi A, Paventi M, Brummer RK, Mohanty B. Modelling of blast-induced stress wave propagation and fracturing in hard rock material. Canadian Institute of Mining (CIM)-Annual Conference; May, 2002; Vancouver, BC, Canada2002.

- [17] Wang ZL, Konietzky H. (2009). Modelling of blast-induced fractures in jointed rock masses. *Engineering Fracture Mechanics*, 76(12), 1945-55. doi:<https://doi.org/10.1016/j.engfracmech.2009.05.004>
- [18] Wang Z, Huang Y, Xiong F. (2019). Three-Dimensional Numerical Analysis of Blast-Induced Damage Characteristics of the Intact and Jointed Rockmass. *Computers, Materials & Continua*, 60(3), 1189 -206.
- [19] Jiang X, Xue Y, Kong F, Gong H, Fu Y, Zhang W. (2023). Dynamic responses and damage mechanism of rock with discontinuity subjected to confining stresses and blasting loads. *International Journal of Impact Engineering*, 172, 104404. doi:<https://doi.org/10.1016/j.ijimpeng.2022.104404>
- [20] Zhang F, Yang L, Hu H, Huang C, Chen S. (2023). Study on the crack propagation behaviour of eccentric uncoupled blasting in a deep-level rock mass. *International Journal of Mining, Reclamation and Environment*, 37(6), 419-40. doi:10.1080/17480930.2023.2213546
- [21] Livermore Software Technology Corporation L. LS-DYNA® Keyword User's Manual R11 Volume II Material Models 2018.
- [22] Ma GW, An XM. (2008). Numerical simulation of blasting-induced rock fractures. *International Journal of Rock Mechanics and Mining Sciences*, 45(6), 966-75. doi:<https://doi.org/10.1016/j.ijrmms.2007.12.002>
- [23] Dehghan Banadaki MM, Mohanty B. (2012). Numerical simulation of stress wave induced fractures in rock. *International Journal of Impact Engineering*, 40-41, 16-25. doi:<https://doi.org/10.1016/j.ijimpeng.2011.08.010>
- [24] Wang J, Yin Y, Esmaili K. (2018). Numerical simulations of rock blasting damage based on laboratory-scale experiments. *Journal of Geophysics and Engineering*, 15(6), 2399-417. doi:10.1088/1742-2140/aacf17
- [25] Holmquist TJ, Johnson GR, Cook WH, editors. A Computational Constitutive Model for Concrete Subjected to Large Strains, High Strain Rates and High Pressures. 14th International symposium, Vol 2; Warhead mechanisms, terminal ballistics; 1993; Arlington, Quebec; Canada: ADPA;.
- [26] Riedel W, Thoma K, Hiermaier S, Schmolinske E, editors. Penetration of Reinforced Concrete by BETA-B-500 Numerical Analysis using a New Macroscopic Concrete Model for Hydrocodes. 9th international symposium on interaction of the effects of munitions with structures; 1999; Berlin, Germany.
- [27] Wang Z, Wang H, Wang J, Tian N. (2021). Finite element analyses of constitutive models performance in the simulation of blast-induced rock cracks. *Computers and Geotechnics*, 135, 104172. doi:<https://doi.org/10.1016/j.compgeo.2021.104172>
- [28] Xie LX, Lu WB, Zhang QB, Jiang QH, Chen M, Zhao J. (2017). Analysis of damage mechanisms and optimization of cut blasting design under high in-situ stresses. *Tunnelling and Underground Space Technology*, 66, 19-33. doi:<https://doi.org/10.1016/j.tust.2017.03.009>
- [29] Yi C, Sjöberg J, Johansson D. (2017). Numerical modelling for blast-induced fragmentation in sublevel caving mines. *Tunnelling and Underground Space Technology*, 68, 167-73. doi:<https://doi.org/10.1016/j.tust.2017.05.030>
- [30] Borrvall T, Riedel W, editors. The RHT concrete model in LS-DYNA. 8th European LS-DYNA users conference; 2011; Strasbourg, Austria.
- [31] ORICA. (2018). Technical data sheet - Fortis Extra System - Africa.

- 
- [32] Lee EL, Hornig HC, Kury JW. *Adiabatic Expansion Of High Explosive Detonation Products*. United States; 1968. Contract No.: UCRL-50422.
- [33] Hansson H. *Determination of properties for emulsion explosives using cylinder expansion tests and numerical simulation*. Swebrec - Swedish Blasting Research Centre; 2009. Report No.: ISSN 1653-5006.
- [34] Hustrulid WA. *Blasting Principles for Open Pit Mining*: CRC Press; 1999.
- [35] Dotto MS, Pourrahimian Y, Joseph T, Apel D. (2022). Assessment of blast energy usage and induced rock damage in hard rock surface mines. *CIM Journal*, 13(4), 166-80. doi:10.1080/19236026.2022.2126924
- [36] Chen SG, Zhao J. (1998). A study of UDEC modelling for blast wave propagation in jointed rock masses. *International Journal of Rock Mechanics and Mining Sciences*, 35(1), 93-9. doi:[https://doi.org/10.1016/S0148-9062\(97\)00322-7](https://doi.org/10.1016/S0148-9062(97)00322-7)
- [37] Ismail MA, Gozon JS. (1987). Effects of discontinuities on fragmentation by blasting. *International Journal of Surface Mining, Reclamation and Environment*, 1(1), 21-5. doi:10.1080/09208118708944098
- [38] Yang R, Ding C, Yang L, Chen C. (2018). Model experiment on dynamic behavior of jointed rock mass under blasting at high-stress conditions. *Tunnelling and Underground Space Technology*, 74, 145-52. doi:<https://doi.org/10.1016/j.tust.2018.01.017>
- [39] Saadatmand Hashemi A, Katsabanis P. (2020). The Effect of Stress Wave Interaction and Delay Timing on Blast-Induced Rock Damage and Fragmentation. *Rock Mechanics and Rock Engineering*, 53(5), 2327-46. doi:10.1007/s00603-019-02043-9
- [40] WipWare. *Sampling and Analysis Guide*2021.
- [41] Cui J, Xie L, Qiao W, Qiu L, Hu Z, Wu L. (2022). Study on blasting characteristics of rock mass with weak interlayer based on energy field. *Scientific Reports*, 12(1), 12698. doi:10.1038/s41598-022-17028-y